ORIGINAL RESEARCH ARTICLE

Simulation of Material Flow Behavior during Friction Stir Welding of 7075 Aluminum Alloy

Defen Zhang, Peigang Jiang, Qiyuan Tang, Yang Lv, Qingzhen Ran, and Xiaowen Chen

The properties of friction stir welding (FSW) joints are affected by three factors: high temperature, material flow and microstructure change. For material flow, it is difficult to carry out experiments alone. Therefore, based on Deform3D software, this paper studies the flow of materials in the horizontal and thickness directions during FSW of 7075 aluminum alloy. The results show that the material flow patterns are different in the horizontal and thickness directions. In the horizontal direction, most of the materials on the advancing side (AS) flow around the stirring pin and finally deposit behind the AS. In the thickness direction, the closer to the upper surface, the more intense the material flow; the materials within the influence range of the stirring needle will basically follow the stirring needle to move upward and deposit behind the stirring head.

1. Introduction

FSW is a mature and novel solid-state welding technology. It involves temperature, mechanics, metallurgy and interaction. It has become a revolutionary welding technology because of its energy saving, environmental protection and high-quality welding (Ref 1-4). And the state-of-the-art friction-based welding techniques are characterized by low peak temperature, severe plastic deformation, energy efficiency and nonpollution, which can simultaneously realize the mechanical and chemical bonding, improving mechanical performances (Ref 5). Compared with the traditional fusion welding process, there is no metal melting phenomenon in the FSW process, which can perfectly avoid common defects such as pores and cracks, and the joints obtained by FSW also have excellent characteristics such as small residual stress and deformation and dense structure (Ref 6-8). After 30 years of development, FSW has shown good benefits in economy and technology. It has great application prospects in the field of national defense and industrial manufacturing (Ref 9, 10).

Due to the influence of material flow, FSW joints produce defects such as flash, void, and tunnels (Ref 11, 12), and their internal microstructures are usually different, resulting in differences in their mechanical properties. Therefore, it is of

great significance to study the material flow in the FSW process to improve the quality of FSW joints. In order to optimize the process parameters, the whole process of FSW is simulated, including computational fluid dynamics model and computational solid mechanics model (Ref 13, 14). High-throughput screening method, based on the marriage between massively parallel computational methods and existing database containing the calculated properties, is capable to explore hypothetical candidates, and the amelioration via the material flow model inhibits the welding defects and optimizes the parameter intervals, providing references to extracting process–structure–property linkages for FSW (Ref 15).

Dialami et al. (Ref 16) established a rigid tool model in the Lagrangian framework and used the material particle tracking method to simulate the effects of different parameters on the defects in the FSW process. Qin et al. (Ref 17) combined experimental methods with numerical simulation to study the flow behavior of 2024 aluminum alloy sheet material during high-speed FSW. The results show that at high rotation speed, the flow distance of the plastic metal on both sides along the welding direction and the transverse flow distance of the retreating side (RS) along the weld center line are shorter. Sun et al. (Ref 18) developed a three-dimensional transient computational fluid dynamics model to study the effects of smooth pins and pitches of 1,2, and 3 mm on the material flow during FSW. Gao et al. (Ref 19) established a finite element model of FSW based on solid mechanics by using ABAQUS software and studied the material flow in FSW process by using tracer particle technology. The simulation results show that the flow pattern of tracer particles around the stirring needle is spiral motion. Luo et al. (Ref 20) used Deform software to simulate the same results. Many scholars have simulated the influence of different pin shapes on the material flow (Ref 21, 22). The experimental results show that the joints with better material flow obtain better mechanical properties.

In practical applications, the material flows to form the weld joint under the action of high temperature and stirring head, but the flow inside the material is not easy to observe, it is of great convenience to observe the material flow in the FSW process

Defen Zhang and Peigang Jiang, State Key Laboratory of Oil and Gas Reservoir Geology and Exploitation(Southwest Petroleum University), Chengdu 610500 Sichuan, China; and School of New Energy and Materials, Southwest Petroleum University, Chengdu 610500 Sichuan, China; Qiyuan Tang, Yang Lv, Qingzhen Ran, and Xiaowen Chen, School of New Energy and Materials, Southwest Petroleum University, Chengdu 610500 Sichuan, China. Contact e-mail: 574285778@qq.com.

by numerical simulation. In this paper, based on the coupled Euler–Lagrange (CEL) method, a FSW model of 7075 aluminum alloy was established. Combined with the thermal cycle curve and strain distribution, the different flow behaviors of the material in the horizontal and thickness directions were comprehensively analyzed. The numerical model accurately predicts the occurrence of void defects at the top of NZ on the AS and is verified by experiments. The model is of great significance for optimizing welding process parameters and improving joint quality.

2. Establishment of Finite Element Model

2.1 Physical Model and Meshing

In this paper, a quasi-steady-state numerical model of FSW of 7075 aluminum alloy is established by using Deform software. The CEL calculation method is used, which can improve the distortion problem in the ordinary grid model to the greatest extent. The size of the aluminum alloy plate used in the simulation is $100 \times 60 \times 5$ mm; the stirring head adopts a flat shoulder and a smooth conical stirring needle. The size and relative position of the stirring head are shown in Fig. 1. In the simulation, the stirring head is a rigid tool. Because the simulated surface of the stirring head is poor after meshing, the stirring head does not divide the grid. The aluminum alloy workpiece is set as a Euler body and is divided by relative grids. At the same time, local refinement is adopted around the stirring head, and the grid moves with the stirring head, as shown in Fig. 2. Therefore, the interface contact between the stirring head and the welded workpiece is a typical fluid-solid coupling setting.
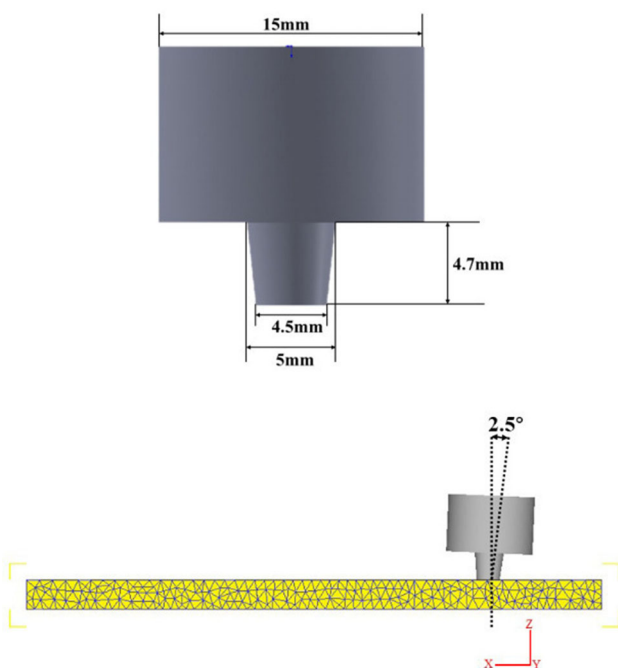
2.2 Material Model

During the FSW process, the material undergoes extrusion and shear deformation under the action of the stirring head and undergoes high temperature and severe plastic deformation. In this paper, the hyperbolic sine equation proposed by Sheppard and Wright et al. (Ref 23) to describe the deformation behavior of materials at high temperature is selected as the constitutive equation of 7075 aluminum alloy material, and its expression form is as follows: Formula (1)

$$\sigma_s = \frac{1}{\alpha} \ln \left\{ \left(\frac{Z}{A} \right)^{1/n} + \left[\left(\frac{Z}{A} \right)^{2/n} + 1 \right]^{1/2} \right\} \qquad \text{(Eq 1)}$$

In the formula, σ_s is the flow stress of material, A, α, n are constants related to materials, Z is the Zener–Hollomon parameter, and the Z parameter is given by formula (2).

$$Z = \dot{\varepsilon} \exp(Q/RT) \qquad \text{(Eq 2)}$$

In the formula, $\dot{\varepsilon}$ is the strain rate, Q is the plastic strain activation energy of material, R is a general gas constant, and T is the absolute temperature. The material parameters of 7075 aluminum alloy are given in Table 1 (Ref 24).

2.3 Boundary Condition

In the process of FSW, the tool and the workpiece are in friction contact with each other. In order to prevent the workpiece from sliding, it is necessary to set appropriate boundary conditions. The bottom surface of the workpiece is constrained in the Z-direction, the four sides are constrained in the XYZ direction, and the upper surface is a free plane without constraints.

There is heat exchange between the upper surface and the side of the workpiece and the air during the FSW process. The
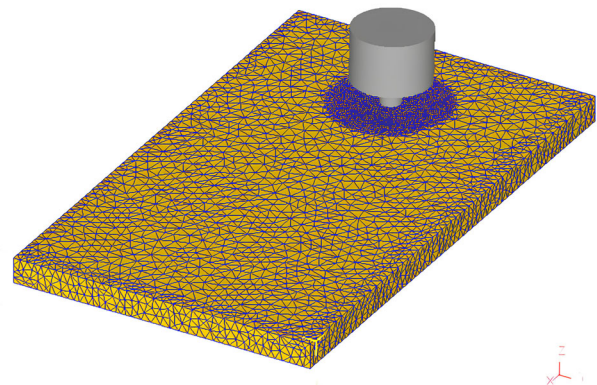

Fig. 2 Part mesh local encryption schematic diagram

Fig. 1 Stirring head size and relative position diagram

Table 1 Constitutive equation parameters of 7075 aluminum alloy

Material	α, Mpa^{-1}	A, s^{-1}	n	Q, J/mol	R, J/mol
7075	0.01	2.69×10^{11}	6.14	158432	8.314

heat transfer coefficient is 20 W/(m^2 K), and the heat transfer between the lower surface and the backing plate is 1000 W/(m^2 K). The initial temperature of the simulation process is set to 20 °C.

In the process of FSW, most of the heat is generated by the friction between the tool and the workpiece, so the contact boundary conditions are necessary. In this paper, shear friction is used as the friction boundary condition between the stirring head and the workpiece. The expression is:

$$F = \mu \cdot \sigma_S \tag{Eq 3}$$

In the formula, F is the friction stress, μ is shear yield stress, σ_S is the shear friction coefficient, this paper takes 0.5

3. Plastic Flow Simulation Results and Analysis

3.1 Material Flow in the Horizontal Direction

In order to visualize the material flow phenomenon, in the Deform post-processing module, and use the Point tracking tool to define the tracer particles, which flow continuously with the welding process, and analyze the material flow in the FSW process by tracking the movement of the tracer particles.

Taking the simulation of process parameters with a rotation speed of 800 rpm and a welding speed of 100 mm/min as an example, in order to fully understand the flow of the material in the horizontal direction, tracking points are set at 13 mm from the starting position of the welding, and the position is in the middle of the starting point and the end point of the welding. The welding process is relatively stable. Three sets of tracking points were set up at the distance of 0.5, 2.5 and 0.5 mm from the upper surface and the lower surface of the weld center, respectively. A point was set every 0.2 mm along the welding direction, a total of 153 points, which were marked as P1-P51,

P52-P102, and P103-P153. The tracking points setting is shown in Fig. 3.

Figure 4 shows the flow of the tracking points on the horizontal plane at different times during the welding process. As the stirring head advances, the tracking points moves backwards along the stirring needle. When $t = 12$ s, the upper surface material begins to flow first, followed by the middle layer and the bottom material. When $t = 13$ s, some tracking points on the upper surface do not move with the stirring pin, but are deposited behind the stirring head, while the middle and bottom tracking points are still attached to the surface of the stirring pin at this time. When $t = 17$ s, most of the tracking points on the upper surface are deposited behind the stirring head. At this time, only a small number of tracking points are still flowing around the stirring needle, while the tracking points on the middle and bottom deposited behind the stirring head are much less than those on the upper surface. When $t = 20$ s, the tracking points of the three parts are finally separated from the rear of the stirring head slightly near the AS, and then deposited, but the tracking points in the upper surface area are farther from the stirring needle area than the middle and lower areas, while the middle area is only slightly farther than the bottom area. Based on the above situation, the material flow on the upper surface is faster than the middle and bottom areas.

Taking the tracking points P51, P102 and P153 representing the upper, middle and lower three regions as an example. As shown in Fig. 5, the displacement–time curve and velocity–time curve of the tracking points P51, P102 and P153 in the Y-direction are obtained. After the three points flow around the stirring pin, the AS position is deposited. Among them, the tracking point P51 is the farthest from the weld center, which is 1.08 mm, followed by P102, which is 0.59 mm from the weld center line, and P153 is the closest to the weld center line, which is 0.54 mm. The material flow velocity of P51 point is the fastest, reaching 16.3 mm/s, and the velocity of P51 and
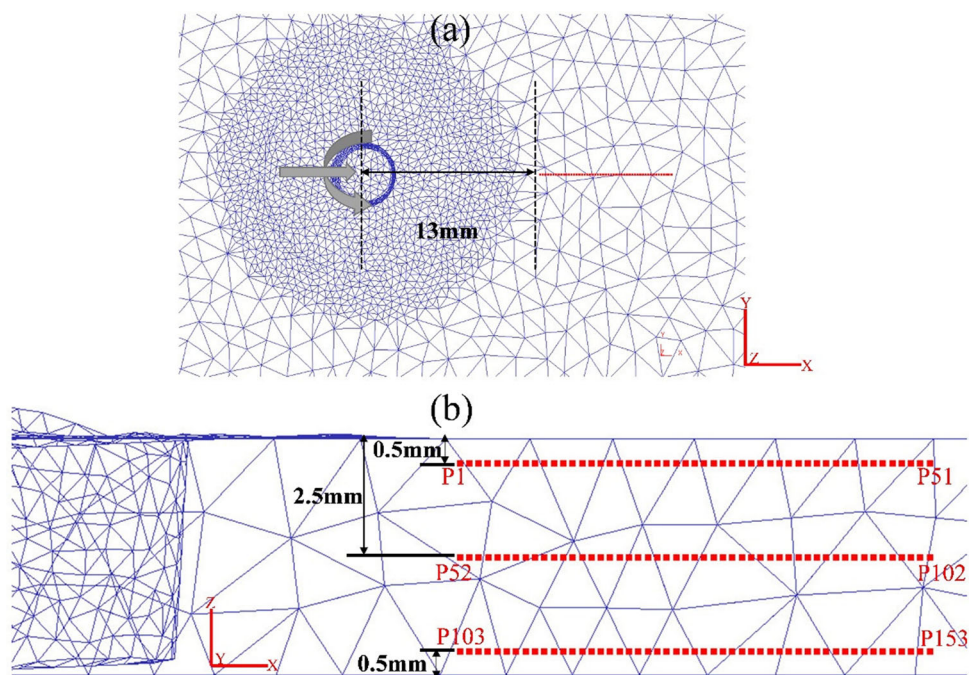

Fig. 3 The initial position of tracking points (a) x-y plane (b) x-z plane
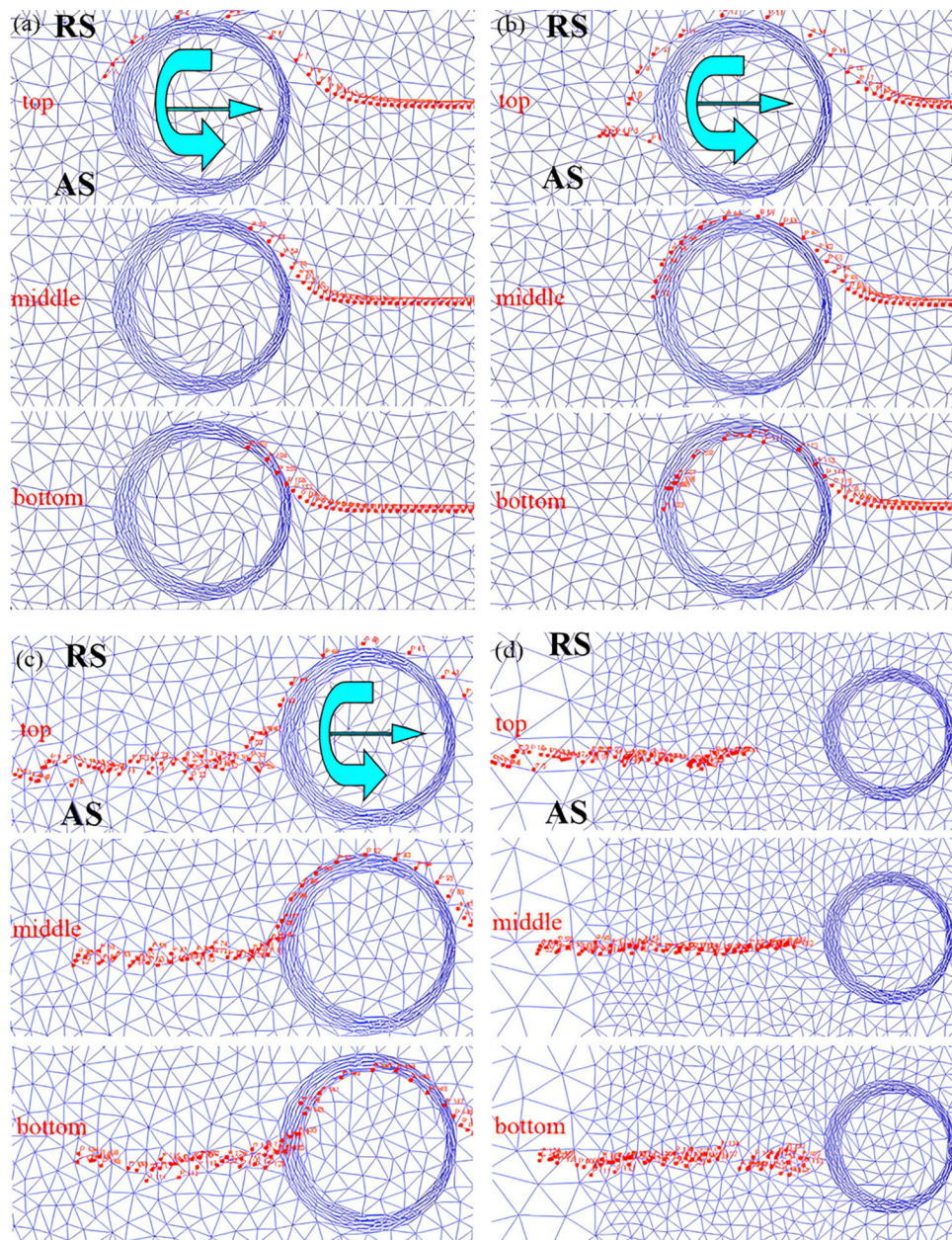
Fig. 4 Horizontal distribution of tracking points at different time points (a) $t = 12$ s (b) $t = 13$ s (c) $t = 17$ s (d) $t = 20$ s

P153 points is 10.6 and 7.4 mm/s, respectively. At the same time, it can be found that the tracking point P51 reaches the peak velocity before the other two points, indicating that the tracking point P51 flows around the needle before the other two points, which is consistent with the results in Fig. 4.

The thermal cycle curve of temperature changing with welding time is shown in Fig. 6. In the figure, the seam center is 13 mm away from the starting point. The temperature is asymmetrically distributed along the weld center, and the temperature on the AS is slightly higher than that on the RS. This is due to the accumulation of materials on the AS, which produces more heat, and the peak temperature appears on the inside of the shoulder edge on the AS. With the increase of the distance from the upper surface of the workpiece, the influence of the shoulder is reduced, the friction heat production area on the side of the stirring needle becomes smaller, and the

temperature decreases. The temperature of the upper surface rises fastest, and the temperature is the highest. The material first enters the plastic state and undergoes severe flow. At the same time, the closer the conical stirring needle is to the upper surface, the larger the diameter of the stirring needle, the greater the linear velocity of the material around the stirring needle, and the faster the flow velocity of the material (Ref 25).

In order to more conveniently understand the flow of the material in the horizontal direction, taking the material 0.5 mm from the upper surface as an example, tracking points are set at 13 mm in front of the stirring head, and the tracking points are set as shown in Fig. 7. The tracking points are set at a horizontal interval of 0.5 mm, from the AS P1 point at 20 mm from the weld center to the symmetrical RS P40 point, a total of 40 tracking points are set.
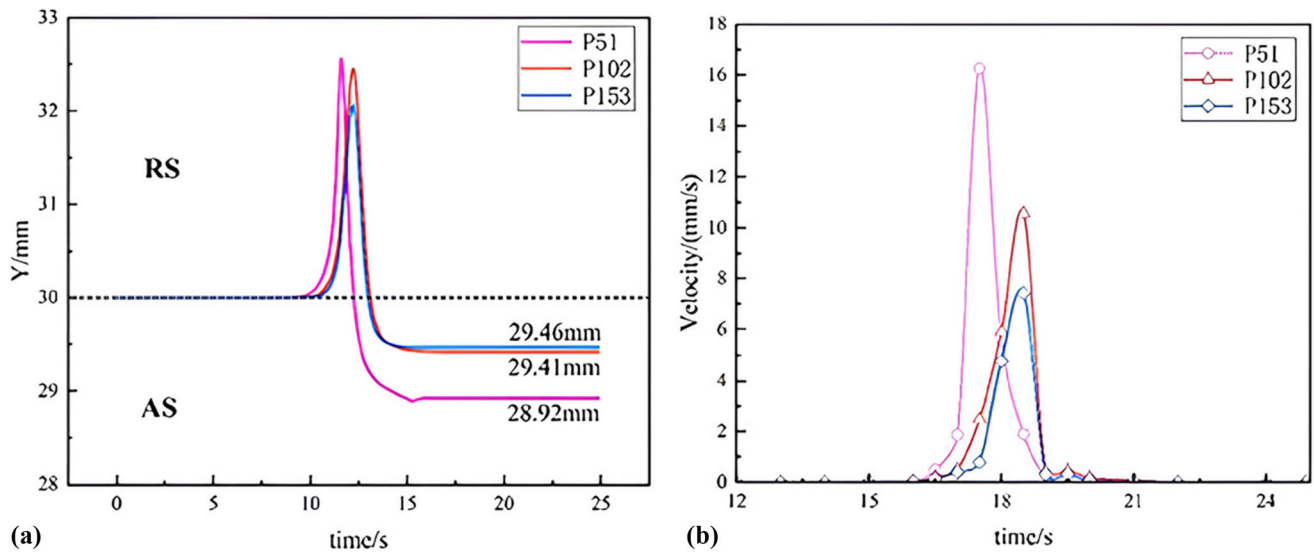
(a)

(b)

Fig. 5 P51, P102, P153 tracking points Y-direction displacement change and velocity change (a) Y-direction displacement change (b) velocity change
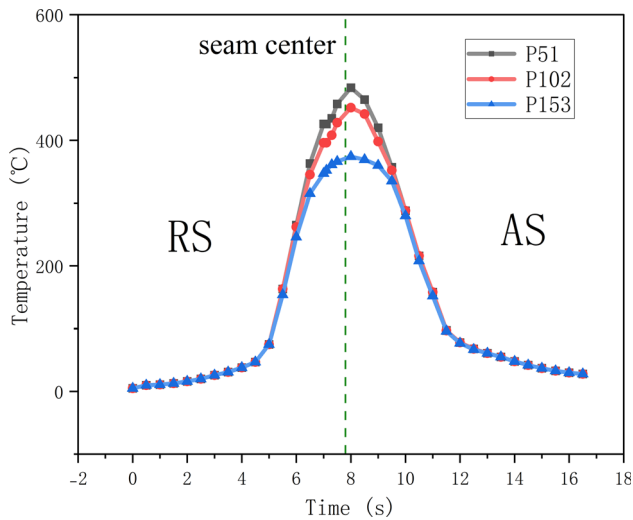

Fig. 6 Thermal cycling curves of P51, P102 and P153

Figure 8 shows the flow of tracking points at different times during FSW. At $t = 11.5$ s, the tracking points on the RS first followed the stirring needle, and the points in the middle position also followed the flow at this time. As the stirring head continues to move forward, more points on the AS follow the stirring head flow; when $t = 14$ s, the P17 point followed the stirring needle to flow around for nearly a circle, and finally deposited behind the AS of the stirring head. At the same time, it is evident that most of the tracking points on the RS basically crossed the weld center line slightly to the rear of the AS. When the welding is completed, the tracking points near the shoulder edge of the AS flows forward slightly under the action of the shoulder. This is because the shoulder edge has a large linear velocity, which causes the material flow to accelerate and the tracking points to move forward. The tracking points near the stirring needle migrate under the action of the stirring needle, and the tracking points from the edge of the stirring needle on the AS to the edge of the shaft shoulder are arranged in a slightly smaller ' U ' shape. However, this phenomenon was

not observed on the RS, indicating that the material flow was more intense on the AS. Figure 9 shows the plastic strain distribution of the cross section during welding. It is clear that the equivalent plastic strain on the AS is greater than that on the RS, which further confirms that the deformation of the material on the AS is more severe.

In Fig. 8(d), there is also a narrow area of a small number of tracking points (black circle area) at the top of weld nugget zone(NZ) on the AS. In this area, almost only a small number of tracking points exist. It can be recognized that there are obvious material flow differences at different positions of the weld. The abnormal material flow in this area may be the cause of the formation of void defect. The material flow ability at the top of NZ on the AS is the best, which leads to the formation of instantaneous void. It can be seen from Fig. 8(d) that there is no material on the RS flowing into the black circle area, which is formed to coordinate the deformation and flow of the material. Therefore, the preferential formation of void defect at the top of NZ on the AS can be attributed to the instantaneous occurrence of void and insufficient inflow of materials. With the increase in welding speed, the flow velocity and extrusion force in this area decrease, and the probability of void defect in this area increases (black circle area) (Ref 26-28).

3.2 Material Flow in the Thickness Direction

Taking the simulation of process parameters with a rotation speed of 800 rpm and a welding speed of 100 mm/min as an example, the flow of materials in the thickness direction is analyzed. Tracking points are set at a distance of 13 mm from the start of welding. Starting from the upper surface, tracking points are set every 0.5 mm, a total of 10 points. A total of 5 sets of tracking points were set on the center line and both sides of the weld, and the interval between each set of tracking points was 1.5 mm. The distribution of tracking points is shown in Fig. 10.

The flow of the weld center tracking points in the thickness direction is shown in Fig. 11. The tracking points near the upper surface first flows from the center of the weld to the RS. This is because the shape of the stirring needle is conical, and
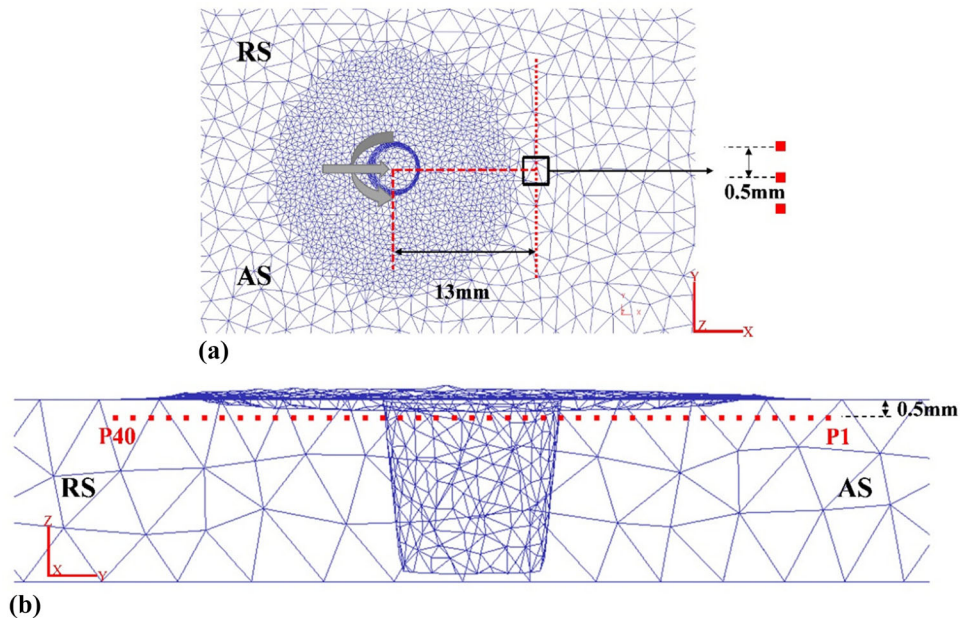
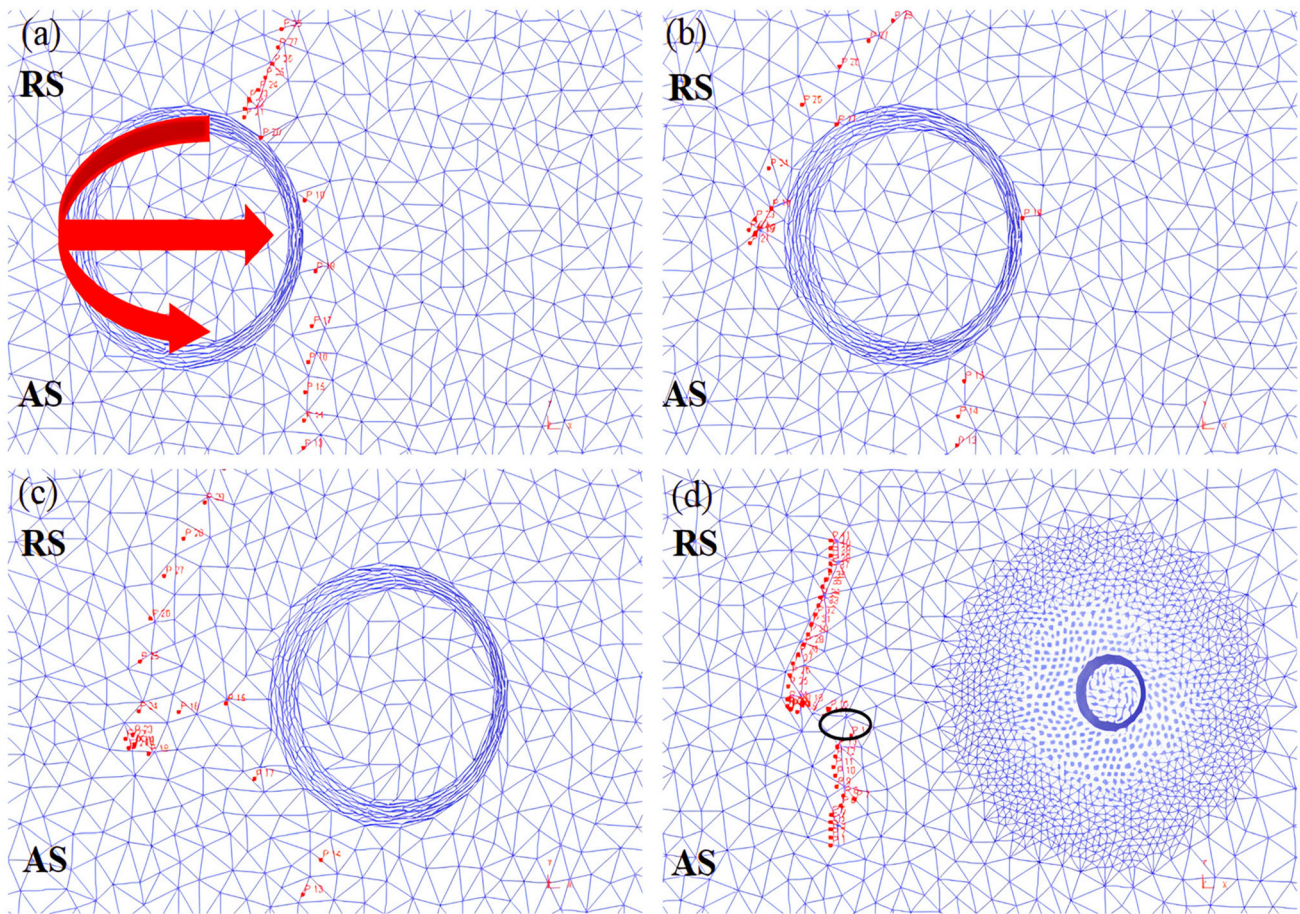**Fig. 7** The initial position of tracking points (a) x-y plane (b) y-z plane

Fig. 8 Distribution of tracking points at different times (a) t = 11.5 s (b) t = 12 s (c) t = 14 s (d) End of welding

the upper radius is larger than the lower part. The linear velocity at the edge of the stirring needle is also larger, and the material flow is more intense. The stirring head continues to

move, and the tracking points P2, P3, and P4 flow into the upper surface of the material through the RS around the stirring needle, indicating that the material is squeezed at this position.
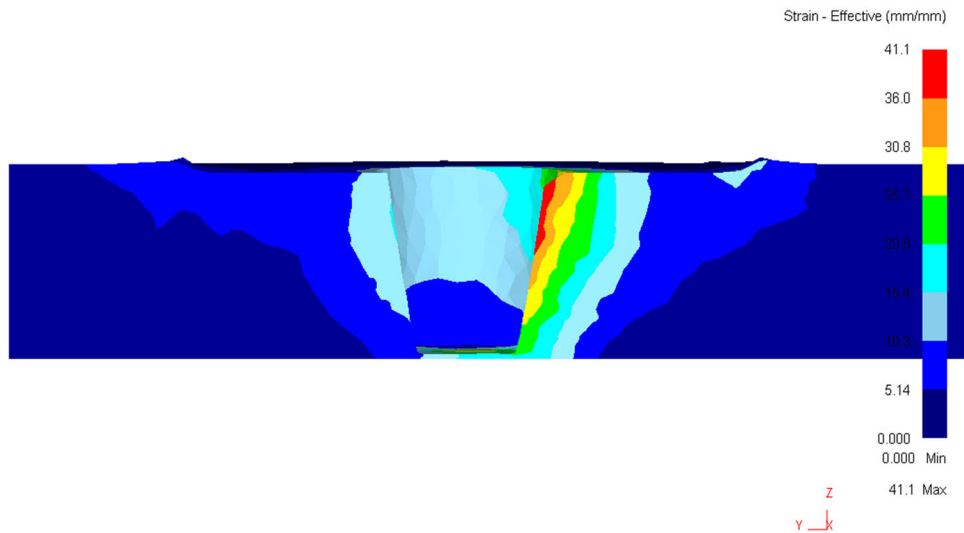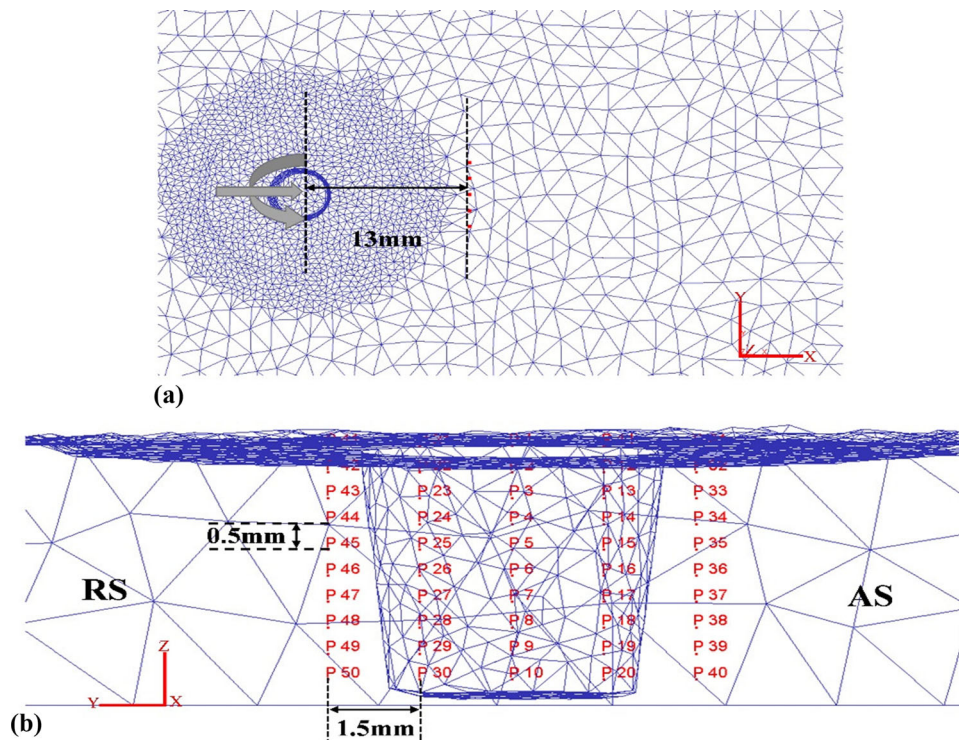
Fig. 9 Equivalent plastic strain distribution

Fig. 10 The distribution diagram of tracing points in the thickness direction (a) x-y plane (b) y-z plane

At the same time, the traction of the stirring needle causes the material to flow upward. In the rear of the stirring needle, due to the weakening of the traction effect and the backward inclination of the stirring head, the tracking points P3 and P4 finally flow downward for a short distance.

The flow distribution of the tracking points on the AS and the RS is shown in Fig. 12. Figure 12(a), (b), (c) and (d) is the flow of the tracking points on the RS, and Fig. 12(e), (f), (g) and (h) is the flow of the tracking points on the AS. Both the left and right figures are the flow at the same time. The tracking points of P21-P30 are 1.5 mm away from the weld, and the tracking points of the RS of P41-P50 are 3 mm away from the weld center line. It is obvious that the tracking points on the RS

of the two groups are near the upper surface. The tracking points near the upper surface have stronger fluidity. Near the upper surface, the larger the radius of the stirring needle, the wider the influence range, and the influence of the shoulder, thus showing stronger fluidity. However, there are still differences between the two groups of tracking points. The flow of the tracking points near the stirring pin is obviously more intense. Among them, P22 and P23 show obvious upward flow behavior, while P42 and P43 at 3 mm from the center of the weld have no obvious upward flow behavior. The flow of the tracking points near the bottom of the material is far less intense than that of the upper tracking points. The bottom tracking points fail to cross the weld center line and enter the
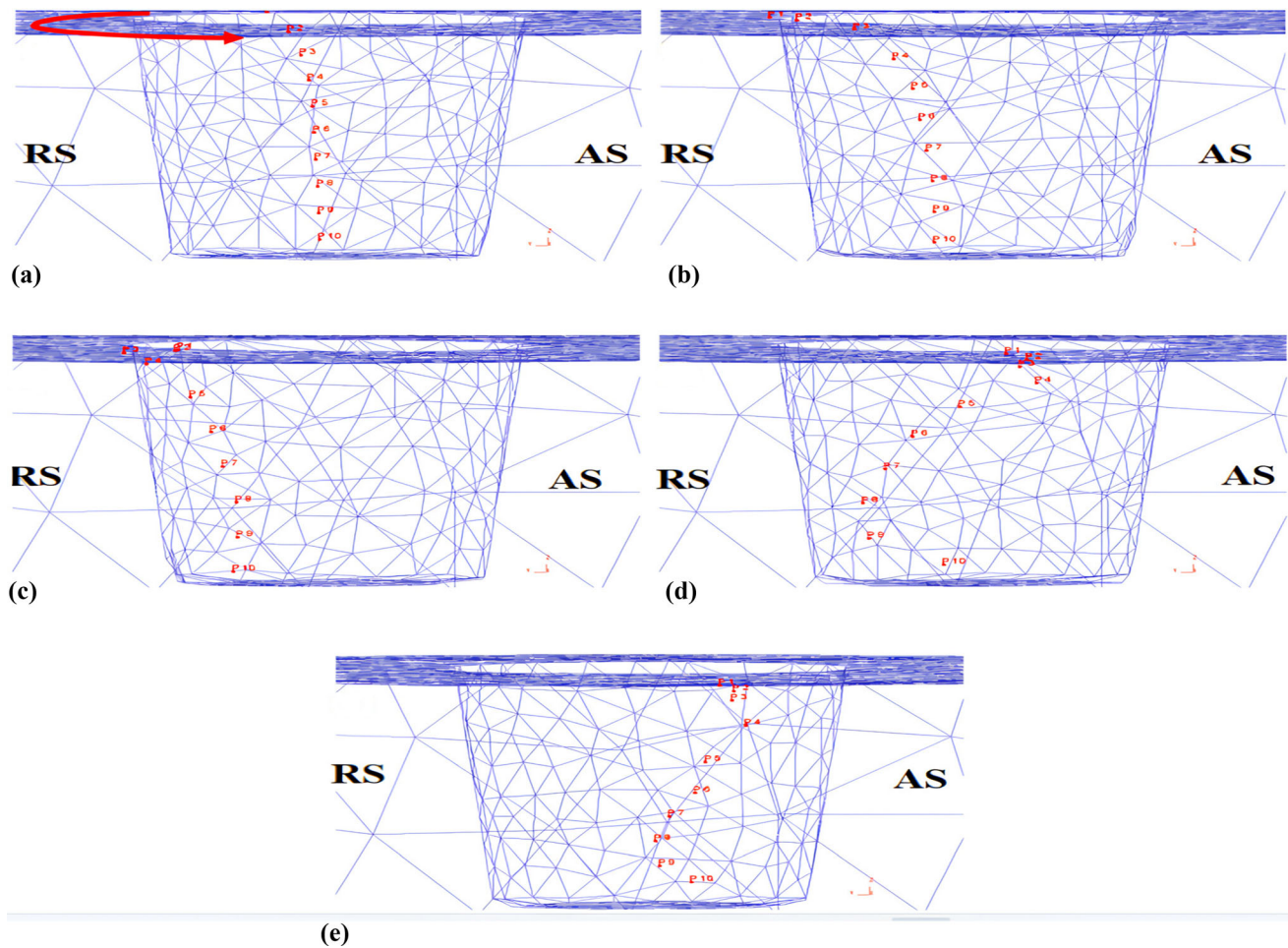
Fig. 11 The distribution map of tracking points at different times on the weld center line (a) initial time (b) $t = 11.5$ s (c) $t = 11.8$ s (d) $t = 12.8$ s (e) final state

AS due to the insufficient traction of the stirring needle. This phenomenon is most obvious at the tracking points 3 mm from the weld center line.

The flow of the material on the AS in the thickness direction is obviously much more intense. Except for P11 and P20, the tracking points of 1.5 mm from the weld center line on the AS have obvious upward flow around the stirring needle, especially P18 point, which flows upward around the stirring needle first, and then moves downward after the stirring needle flows to the rear of the stirring needle. The final deposition position is obviously upward compared with the initial position. However, at the tracking points 3 mm away from the weld center, some materials still follow the stirring needle into the RS and finally deposit on the tail of the AS of the stirring needle. The material at the bottom of the stirring needle has almost no large-scale upward or downward flow due to the weakening of the stirring effect.

As shown in Fig. 13(a), the displacement of P5, P15, P25, P35 and P45 tracking points 2 mm from the upper surface of the weld, which are located at the center line, AS and RS of the weld, respectively, with time along the thickness direction is studied. The P15 point on the AS has the largest displacement change and the longest flow distance. Finally, it is deposited above the initial position of 1.37 mm. (In Fig. 13b, the dotted

line parallel to the X-direction is the initial position.) The displacement of P5 and P25 points at the center line of the weld and the AS of 3 mm from the center line of the weld is the second, but finally due to the decrease of the extrusion force and the backward inclination of the stirring head, the deposition position and the initial position in the thickness direction change little. The two points at 1.5 mm and 3 mm from the center line of the weld also follow the upward flow of the stirring needle, but the final flow is insufficient, and it is deposited below the initial position in the thickness direction. Therefore, it is apparent that there is a clear gap between the AS and the RS in the thickness direction. The AS flows upward with the stirring needle due to the strong shear effect, and most of the tracking points flow into the back of the stirring needle and move slightly downward under the downward extrusion force.

4. Experimental Validations

Figure 14 shows the metallographic structure of FSW of 7075 aluminum alloy with the same size and parameters as the simulation; there is a clear boundary between the NZ on the AS
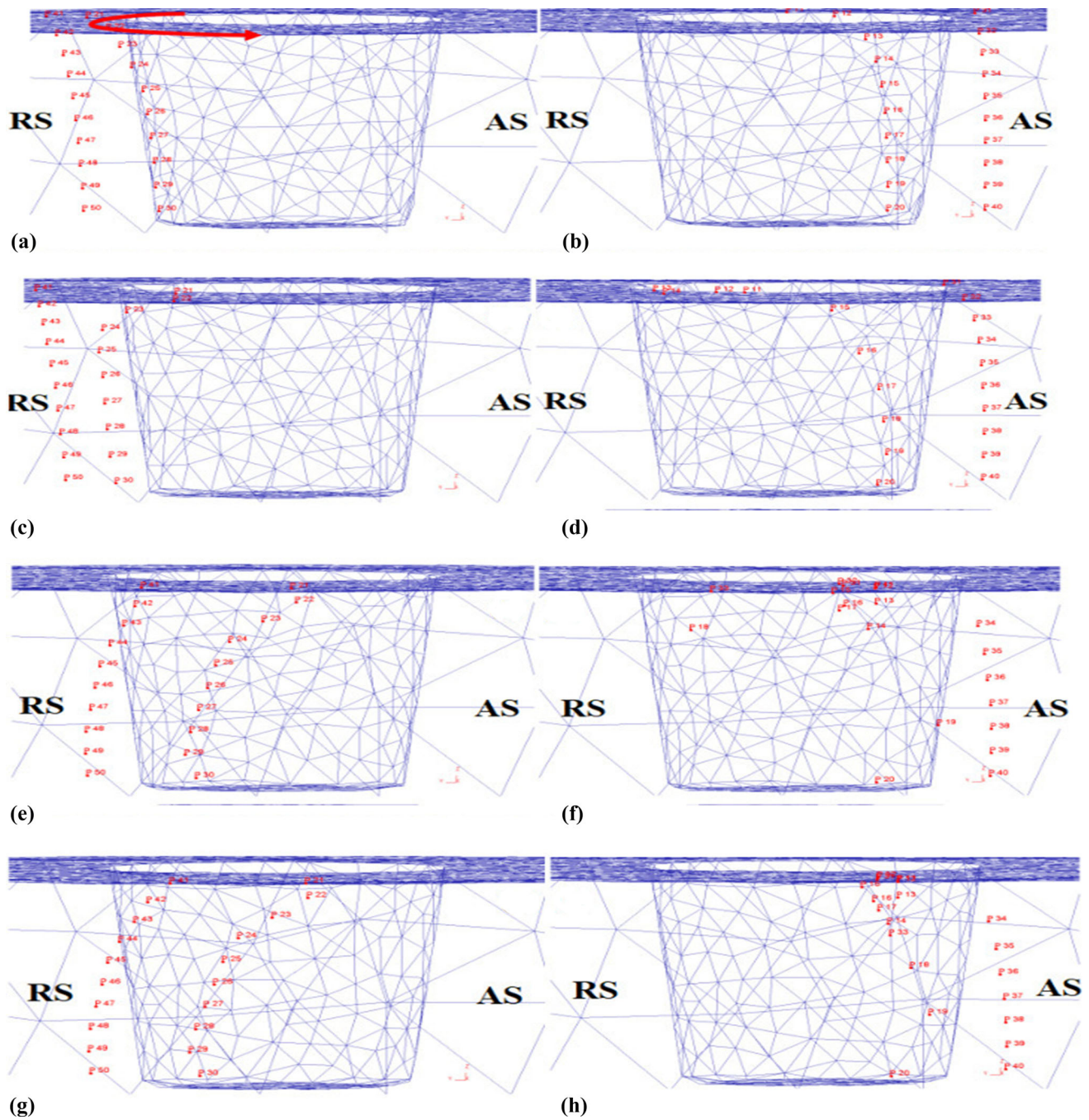
Fig. 12 Diagram of tracking points flow on AS and RS (a)–(d) tracking points flow on RS (e–h) tracking points flow on AS

and the thermo-mechanically affected zone. There are obvious differences in the grain morphology between the two regions; the grain force in the AS is elongated, showing a flat strip grain, which verifies that the material flow ability on the AS is the best. There are obvious differences between AS and RS, and the number of fine grains around RS is more, which proves that there are obvious differences in material flow at different positions of the weld. It is evident that the number of fine grains decreases step by step in the position away from the NZ, that is,

the recrystallization area decreases significantly. However, the boundary between the NZ on the RS and the thermo-mechanically affected zone is not obvious. The farther the distance from the NZ is, the less the number of fine recrystallized grains is, but the change is far less obvious than that of AS, but closer to the process of gradual change, which further confirms that the deformation of the material on the AS is more intense. It was also found that the NZ on the AS had void defects (black circle area).
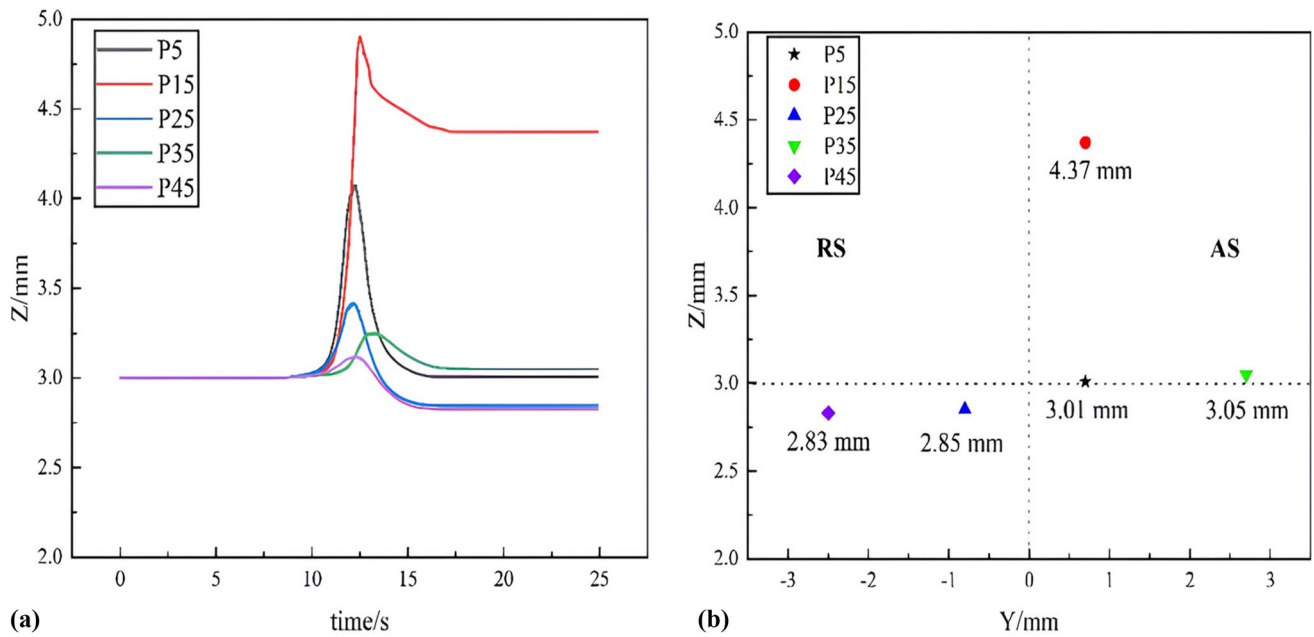
Fig. 13 P5, P15, P25, P35, P45 tracking points in the thickness direction of the displacement and the final position (a) along the thickness direction of the displacement change (b) tracking points on the Y-Z section of the final position
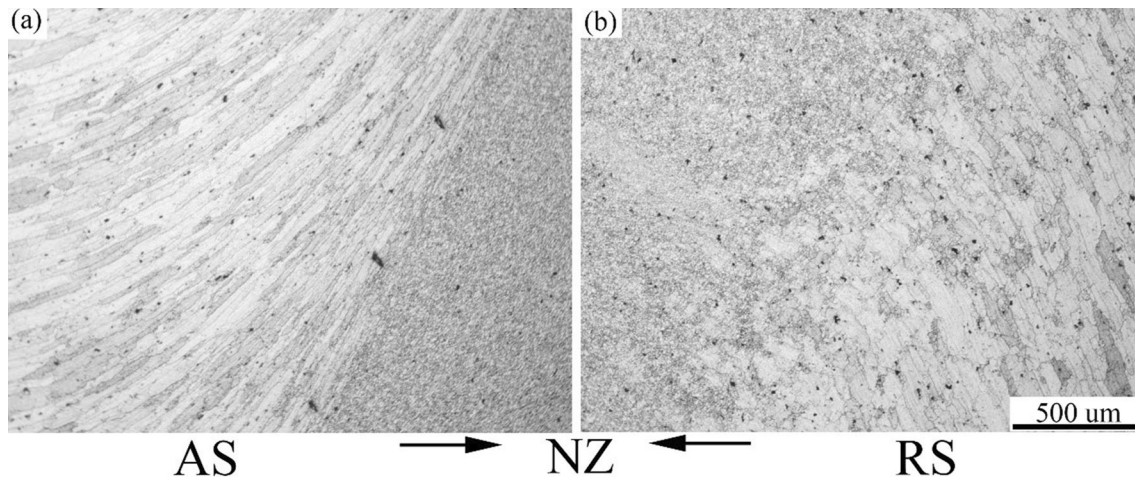

Fig. 14 At 800 rpm-100 mm/min, the metallographic structure of the AS and the RS (a) the AS (b) the RS

5. Conclusions

This study deals with numerical investigation on material flow pattern in FSW of 7075 aluminum alloy.

(1) The material flow patterns are different in the horizontal and thickness directions.
(2) In the horizontal direction, most of the materials on the AS within the influence of the stirring pin flow around the stirring pin and finally deposit behind the AS.
(3) Void defects occur at the top of NZ on the AS.
(4) In the thickness direction, the closer to the upper surface, the more intense the material flow. The materials within the influence range of the stirring needle will basically follow the stirring needle to move upward and deposit behind the stirring head.

(5) At the position near the stirring needle, the plastic deformation of the AS is more severe than that of the RS, and the material flow is more intense.

Conflict of interest

The authors declare that they have no known competing financial interests or personal relationships that could have appeared to influence the work reported in this paper.

Reference

1. R.V. Marode, S.R. Pedapati, and T.A. Lemma et al., A Review on Numerical Modelling Techniques in Friction stir Processing: Current and Future Perspective, *Archiv. Civ. Mech. Eng.*, 2023, **23**, p 154. https://doi.org/10.1007/s43452-023-00688-6

2. J. Hirsch, Recent Development in Aluminium for Automotive Applications, *Transact. Nonferrous Mater. Soc. China*, 2014, **24**(7), p 1995–2002. https://doi.org/10.1016/S1003-6326(14)63305-7

3. T. Dursun and C. Soutis, Recent Developments in Advanced Aircraft Aluminium Alloys, *Mater. Design*, 2014, **56**, p 862–871. https://doi.org/10.1016/j.matdes.2013.12.002

4. X. Meng, Y. Huang, and J. Cao et al., Recent Progress on Control Strategies for Inherent Issues in Friction Stir Welding, *Prog. Mater. Sci.*, 2021, **115**, 100706. https://doi.org/10.1016/j.pmatsci.2020.100706

5. X. Meng, Y. Xie, and S. Sun et al., Lightweight Design: Friction-Based Welding Between Metal and Polymer, *Acta Metall. Sin.*, 2023 https://doi.org/10.1007/s40195-023-01552-5

6. J.G. Li and S.Q. Wang, Distortion Caused by Residual Stresses in Machining Aeronautical Aluminum Alloy Parts: Recent Advances, *Int. J. Adv. Manuf. Technol.*, 2017, **89**, p 997–1012. https://doi.org/10.1007/s00170-016-9066-6

7. A.K. Choudhary and R. Jain, Numerical Prediction of Various Defects and Their Formation Mechanism During Friction Stir Welding Using Coupled Eulerian-Lagrangian Technique, *Mech. Adv. Mater. Struct.*, 2023, **30**(12), p 2371–2384. https://doi.org/10.1080/15376494.2022.2053911

8. Y. Li, W. Zou, and B. Lee et al., Research Progress of Aluminum Alloy Welding Technology, *Int. J. Adv. Manuf. Technol.*, 2020, **109**(5–6), p 1207–1218. https://doi.org/10.1007/s00170-020-05606-1

9. L.E. Murr, A Review of FSW Research on Dissimilar Metal and Alloy Systems, *J. Mater. Eng. Perform.*, 2010, **19**(8), p 1071–1089. https://doi.org/10.1007/s11665-010-9598-0

10. R.S. Mishra and Z.Y. Ma, Friction Stir Welding and Processing, *Mater. Sci. Eng. R. Rep.*, 2005, **50**(1), p 1–78. https://doi.org/10.1016/j.mser.2005.07.001

11. M. Türkan and Ö. Karakaş, Numerical Modeling of Defect Formation in Friction Stir Welding, *Mater. Today Commun.*, 2022, **31**, p 103539. https://doi.org/10.1016/j.mtcomm.2022.103539

12. X.C. Liu and C.S. Wu, Elimination of Tunnel Defect in Ultrasonic Vibration Enhanced Friction Stir Welding, *Mater. Des.*, 2016, **90**, p 350–358. https://doi.org/10.1016/j.matdes.2015.10.131

13. Y. Xie, X. Meng, and Y. Huang, Entire-Process Simulation of Friction Stir Welding—Part 1: Experiments and Simulation, *Weld. J.*, 2022, **5**, p 144. https://doi.org/10.29391/2022.101.011

14. Y. Xie, X. Meng, and Y. Huang, Entire-Process Simulation of Friction Stir Welding—Part 2: Implementation of Neural Networks, *Weld. J.*, 2022, **101**, p 172–177. https://doi.org/10.29391/2022.101.013

15. Y. Huang, Y. Xie, and X. Meng et al., Joint formation mechanism of high depth-to-width ratio friction stir welding, *J. Mater. Sci. Technol.*, 2019, **35**(7), p 1261–1269. https://doi.org/10.1016/j.jmst.2019.01.016

16. N. Dialami, M. Cervera, and M. Chiumenti, Defect Formation and Material Flow in Friction Stir Welding, *Eur. J. Mech. A. Solids*, 2020, **80**, 103912. https://doi.org/10.1016/j.euromechsol.2019.103912

17. D.Q. Qin, L. Fu, and Z.K. Shen, Visualisation and Numerical Simulation of Material Flow Behaviour During High-Speed FSW Process of 2024 Aluminium Alloy Thin Plate, *Int. J. Adv. Manuf. Technol.*, 2019, **102**, p 1901–1912. https://doi.org/10.1007/s00170-018-03241-5

18. Z. Sun and C.S. Wu, Inf6luence of Tool Thread Pitch on Material Flow and Thermal Process in Friction Stir Welding, *J. Mater. Process. Technol.*, 2020, **275**, p 116281. https://doi.org/10.1016/j.jmatprotec.2019.116281

19. E. Gao, X. Zhang, C. Liu et al., Numerical Simulations on Material Flow Behaviors in Whole Process of Friction Stir Welding, *Transact. Nonferrous Metals Soc. China*, 2018, **28**(11), p 2324–2334. https://doi.org/10.1016/S1003-6326(18)64877-0

20. H. Luo, T. Wu, and P. Wang et al., Numerical Simulation of Material Flow and Analysis of Welding Characteristics in Friction Stir Welding Process, *Metals*, 2019, **9**(6), p 621. https://doi.org/10.3390/met9060621

21. M. Mirzaei, P. Asadi, and A. Fazli, Effect of Tool Pin Profile on Material Flow in Double Shoulder Friction Stir Welding of AZ91 Magnesium Alloy, *Int. J. Mech. Sci.*, 2020, **183**, p 105775. https://doi.org/10.1016/j.ijmecsci.2020.105775

22. R. Jain, S.K. Pal, and S.B. Singh, Finite Element Simulation of Pin Shape Influence on Material Flow, Forces in Friction Stir Welding, *Int. J. Adv. Manuf. Technol.*, 2018, **94**, p 1781–1797. https://doi.org/10.1007/s00170-017-0215-3

23. D.S. Wright and T. Sheppard, Determination of Flow Stress: Part 2 Radial and Axial Temperature Distribution During Torsion Testing, *Metals Technol.*, 1979, **6**(1), p 224–229.

24. T. Sheppard and A. Jackson, Constitutive equations for use in prediction of flow stress during extrusion of aluminium alloys, *Mater. Sci. Technol.*, 1997, **13**(3), p 203–209. https://doi.org/10.1179/mst.1997.13.3.203

25. R. Padmanaban, V. Ratna Kishore, and V. Balusamy, Temperature Distribution and Material Flow During Friction Stir Welding of Dissimilar Aluminum Alloys, *Procedia Eng.*, 2014, **97**, p 854–863. https://doi.org/10.1016/j.proeng.2014.12.360

26. W.J. Arbegast, A Flow-Partitioned Deformation Zone Model for Defect Formation During Friction Stir Welding, *Scripta Mater.*, 2008, **58**(5), p 372–376. https://doi.org/10.1016/j.scriptamat.2007.10.031

27. X.H. Zeng, P. Xue, and D. Wang et al., Material Flow and Void Defect Formation in Friction Stir Welding of Aluminium Alloys, *Sci. Technol. Weld. Join.*, 2018, **23**(8), p 677–686. https://doi.org/10.1080/13621718.2018.1471844

28. M. Al-Moussawi, A.J. Smith, A. Young, S. Cater, and M. Faraji, Modelling of Friction Stir Welding of DH36 Steel, *Int. J. Adv. Manuf. Technol.*, 2017, **92**, p 341–360. https://doi.org/10.1007/s00170-017-0147-y